

Multi-wavelength Emission of Gamma-ray Burst Prompt Phase. I. Time-resolved and Time-integrated Polarizations

JIA-SHENG LI,¹ MI-XIANG LAN,¹ AND HAO-BING WANG¹

¹*Center for Theoretical Physics and College of Physics, Jilin University, Changchun, 130012, China; lanmixiang@jlu.edu.cn*

ABSTRACT

The time-integrated polarization degree (PD) at prompt optical band of gamma-ray burst (GRB) was predicted to be less than 20%, while the time-resolved one can reach as high as 75% in photosphere model. Polarizations in optical band during GRB prompt phase had not been studied under framework of the magnetic reconnection model. Here, a three-segment power laws of the energy spectrum is used to reconstruct the Stokes parameters of the magnetic reconnection model. The multi-wavelength light curves and polarization curves from the optical band to MeV gamma-rays in GRB prompt phase are studied. We found depending mainly on the jet dynamics there is a long lasting high PD phase at all calculated energy bands for the typical parameter sets. The time-resolved PD could be as high as 50%, while the time-integrated one is roughly 17% in optical band. It can reach 60% for the time-resolved PD in X-rays and the time-integrated one is around (30–40)%. The polarization angle (PA) evolution is random in both optical and gamma-ray bands for the photosphere model, while it is roughly a constant in the synchrotron models. Therefore, future time-resolved PA observations in the prompt optical or gamma-ray band could distinguish between the photosphere and the synchrotron models.

Keywords: Gamma-ray bursts (629); Magnetic fields (994);

1. INTRODUCTION

Gamma-ray bursts (GRBs) are sudden intensification of gamma rays in the universe. Even if GRB was first detected in 1967, there are still many mysteries to solve after decade years of studies. They are divided into long and short bursts depending on whether or not the duration of the prompt-emission phase exceeds 2 s. Long bursts usually result from the collapse of a massive star (Woosley 1993; Bloom et al. 1999; MacFadyen et al. 2001; Mazzali et al. 2003; Hjorth et al. 2003), while the short bursts are from the merger of the two compact objects (Narayan et al. 1992; Abbott et al. 2017; Goldstein et al. 2017; Lazzati et al. 2018). For a black hole central engine, Blandford–Znajek mechanism (Blandford & Znajek 1977) would work and the magnetic field configuration (MFC) in the ejecta will be toroidal, while for a magnetar, a stripped wind would be blown out and the MFC in the wind is aligned (Spruit et al. 2001). It was pointed out that the evolution patterns of the polarization angle (PA) will be different for an aligned and a toroidal field in the ejecta during early optical afterglow, so the PA evolution patterns can be used as a probe of the GRB central engine (Lan et al. 2016).

In order to explain the observations of the GRB prompt phase, the internal shock model (Narayan et al. 1992; Rees & Meszaros 1994) and the photospheric model (Thompson 1994; Eichler & Levinson 2000; Mészáros & Rees 2000; Rees & Mészáros 2005; Lazzati et al. 2009; Beloborodov 2011; Pe’er & Ryde 2011; Mizuta et al. 2011; Nagakura et al. 2011; Xu et al. 2012; Ruffini et al. 2013; Bégué et al. 2013; Lundman et al. 2013; Lazzati et al. 2013) were proposed. In the last decade, the magnetic reconnection model (Giannios 2008; Zhang & Yan 2011; Beniamini & Granot 2016; Granot 2016) also becomes popular. It assumes that the highly magnetized central engine ejects highly magnetized shells and these shells will collide with each other, leading to the magnetic reconnection process (Zhang & Yan 2011). Then the free magnetic energy is released to accelerate the electron to produce the synchrotron radiation.

Lan & Dai (2020) had studied the polarization of the GRB prompt phase under the framework of the magnetic reconnection model. The predicted upper limit of the polarization degree (PD) of the magnetic reconnection model is $\sim 50\%$ around gamma-ray band (Sui & Lan 2024), which is different from a roughly zero polarization in the photosphere model (Lundman et al.

2018). The polarization studies of the above models mainly focused on the energy band above soft X-ray. Then it is extended to the optical band in the photosphere model (Parsotan & Lazzati 2022). The results showed that the time-integrated PD in the optical band for the photosphere model is below 20%, which is higher than the predicted zero polarization in gamma-ray band beyond MeV. However, the optical polarization in GRB prompt phase had not been predicted under the framework of the magnetic reconnection model.

The spectrum of the GRB prompt emission is usually fitted by the empirical formulas, i.e., the Band function (Band et al. 1993), which is a two-segment power laws connected at E_p (the peak of the νF_ν spectrum). Fitting the data from the Fermi Gamma-Ray Burst Monitor (Fermi-GBM), the low-energy photon spectral index of the Band function above energy bands of hard X-ray is indicated to be concentrated around -1 (Yu et al. 2016; Poolakkil et al. 2021), which is inconsistent with the predicted value of -3/2 for the fast-cooling synchrotron emission. Then theoretically Uhm & Zhang (2014) had obtained the value of -1 for the low-energy photon spectral index in a relatively weak decaying magnetic field and it approaches -3/2 when the magnetic field becomes stronger. In a wider energy band down to roughly soft X-ray even to optical band, some studies (Oganesyan et al. 2017, 2018, 2019; Ravasio et al. 2019; Toffano et al. 2021) had suggested that there might be a low-energy break in the GRB spectrum and the break energy (E_b) is around a few keV. They found the photon spectral indices are -2/3 below E_b , -3/2 between E_b and E_p , and -2.3 above the E_p , respectively. And their results support the fast-cooling synchrotron emission as the main radiation mechanism in the GRB prompt phase.

Lan & Dai (2020) used the Band function (Band et al. 1993) to construct the Stokes Parameters to study the polarizations of the γ -rays band in GRB prompt phase. In this paper, a three-segment power-law spectrum is used to rebuild the Stokes Parameters (in Section 2), and the observational energy band can be extended down to the lower optical band. Here, the multi-wavelength (from optical to MeV γ -rays) light curves, polarization curves and time-integrated polarizations in the GRB prompt phase are predicted, and also the influences of the key parameters on the time-resolved and time-integrated polarizations are discussed in Section 3. Finally, our conclusions and discussion are arranged in Section 4.

2. THE MODELS

According to the former studies (Uhm & Zhang 2015, 2016; Uhm et al. 2018), a relativistic jet shell expands along the radial direction from the central engine at redshift z . The electrons are isotropically injected into the shell from the radius r_{on} to r_{off} and emit synchrotron photons in the magnetic field. The emitted photons are also assumed to be isotropic in the comoving frame of the jet shell.

Under framework of the magnetic reconnection model, depending on different MFCs in the radiation region, the jet shell could accelerate (corresponding to an aligned field) or keep as a roughly constant velocity (corresponding to a toroidal field) during GRB phase (Drenkhahn 2002). The bulk Lorentz factor Γ would roughly evolve as a power law with radius (Drenkhahn 2002). It reads

$$\Gamma(r) = \Gamma_0(r/r_0)^s, \quad (1)$$

where r_0 is the normalization radius. It is predicted that $s = 0.35$ for an aligned field in the emitting region (Drenkhahn 2002), which is the parallel latitude circles in the jet surface (Spruit et al. 2001; Lan et al. 2019). While a toroidal field with $s = 0$ is the concentric circles around the jet axis in the jet surface.

In the following, the parameters with superscript “ ’ ” indicate the comoving-frame quantities. The spectral power of the emission from single electron can be expressed as

$$P'_{\nu'}(\nu') = P'_0 H_{en}(\nu'), \quad (2)$$

where P'_0 shows the magnitude and $H_{en}(\nu')$ gives the shape of the photon spectrum. The comoving frequency ν' is $\nu' = \nu(1+z)/\mathcal{D}$. And ν is the observational frequency and $\mathcal{D} = 1/\Gamma(1 - \beta_V \cos \theta)$ is the Doppler factor. β_V is dimensionless velocity of the shell. And θ is the angle between the velocity of the jet element and the line of sight.

The P'_0 reads (Rybicki & Lightman 1979)

$$P'_0 = \frac{3\sqrt{3}}{32} \frac{m_e c^2 \sigma_T B'}{q_e}, \quad (3)$$

where m_e and q_e are the mass and charge of the electron, respectively. c is the speed of light and B' represents the strength of the magnetic field.

$$B'(r) = B'_0(r/r_0)^{-b}, \quad (4)$$

where b is the decay index. Due to the expansion of the jet shell and the magnetic reconnection process, the decay index would be larger than 1 (Drenkhahn 2002).

For the $H_{en}(\nu')$, we assume a three-segment-power-laws spectrum for the single-energy electron to mimic

the energy spectrum of the radiation from the power-law distributed electrons.

$$H_{en}(\nu') = \begin{cases} (\nu'/\nu'_1)^{\alpha_1+1}, & \nu' < \nu'_1, \\ (\nu'/\nu'_1)^{\alpha_2+1}, & \nu'_1 < \nu' < \nu'_2, \\ (\nu'_2/\nu'_1)^{\alpha_2+1}(\nu'/\nu'_2)^{\beta+1}, & \nu' > \nu'_2, \end{cases} \quad (5)$$

where α_1 , α_2 and β are the low-energy, mid-energy and high-energy photon spectral indices, respectively. The ν'_1 and ν'_2 are $\min(\nu'_{cool}, \nu'_{min})$ and $\max(\nu'_{cool}, \nu'_{min})$, respectively. Then ν'_{cool} and ν'_{min} read:

$$\nu'_{cool} = \frac{q_e B' \gamma_{cool}^2 \sin \theta'_B}{2\pi m_e c}, \quad \nu'_{min} = \frac{q_e B' \gamma_{ch}^2 \sin \theta'_B}{2\pi m_e c}, \quad (6)$$

where γ_{ch} and γ_{cool} are the characteristic Lorentz factor of electrons. The θ'_B is the pitch angle of the electrons in the magnetic field.

In Uhm et al. (2018), five variation patterns of γ_{ch} with radius were discussed. After our calculation, there are roughly two evolution profiles of the PD curves for these five γ_{ch} patterns, which correspond to the two peak-energy evolution modes (i.e., the hard-to-soft mode and the intensity-tracking mode). For the i model with hard-to-soft mode, its γ_{ch} can be expressed by

$$\gamma_{ch}(r) = \gamma_{ch}^i (r/r_0)^g, \quad (7)$$

where we take $g = -0.2$ Uhm et al. (2018). For the m model with the intensity-tracking mode, its γ_{ch} reads

$$\gamma_{ch}(r) = \gamma_{ch}^m \times \begin{cases} (r/r_m)^g, & r \leq r_m, \\ (r/r_m)^{-g}, & r \geq r_m, \end{cases} \quad (8)$$

where r_m is normalization radius and we take $g = 1.0$ Uhm et al. (2018). The γ_{cool} reads:

$$\gamma_{cool} = 6\pi \frac{m_e c \Gamma}{\sigma_T B'^2 t}, \quad (9)$$

where t is the dynamical time in the burst source frame and σ_T is the Thomson cross section.

For fast cooling (i.e. $\nu'_{cool} < \nu'_{min}$), $\alpha_1 = -2/3$ and $\beta = -1 - \frac{p}{2}$, where p is the index of the true power-law injected electrons ($N(\gamma_e) \propto \gamma_e^{-p}$). And we take $p = 2.6$ in this paper. Observationally, the fitting result of the Band function in the energy band above hard X-rays for the mid-energy photon spectral index is -1 (Yu et al. 2016; Poolakkil et al. 2021), while it is $-3/2$ when the energy band used for the analysis of the energy spectrum is extended to the optical band (Oganesyan et al. 2017, 2018, 2019; Ravasio et al. 2019;

Toffano et al. 2021). Theoretically, in a decaying magnetic field the photon spectral index is -1 for a relatively weak field, while it approaches $-3/2$ when the magnetic field becomes stronger Uhm & Zhang (2014). So two mid-energy photon spectral indices ($\alpha_2 = -1$ and $\alpha_2 = -3/2$) are considered here. For slow cooling (i.e. $\nu'_{min} < \nu'_{cool}$), $\alpha_1 = -2/3$, $\alpha_2 = -1 - \frac{p-1}{2}$ and $\beta = -1 - \frac{p}{2}$.

The observed flux density f_ν , the Stokes parameters Q_ν and U_ν here are slightly different from that in Lan & Dai (2020).

$$f_\nu = \frac{1+z}{4\pi D_L^2} \int \frac{\mathcal{D}^2}{\Gamma} \frac{c}{4\pi r} N P'_0 H_{en}(\nu') \sin \theta'_B d\phi dt, \quad (10)$$

and

$$Q_\nu = \frac{1+z}{4\pi D_L^2} \int \frac{\mathcal{D}^2}{\Gamma} \frac{c}{4\pi r} N P'_0 H_{en}(\nu') \sin \theta'_B \Pi_p \cos 2\chi_p d\phi dt, \quad (11)$$

and

$$U_\nu = \frac{1+z}{4\pi D_L^2} \int \frac{\mathcal{D}^2}{\Gamma} \frac{c}{4\pi r} N P'_0 H_{en}(\nu') \sin \theta'_B \Pi_p \sin 2\chi_p d\phi dt, \quad (12)$$

where D_L is the luminosity distance of the source and $N = \int R_{inj} dt / \Gamma$ is the isotropic total electron number in the shell. The ϕ is the angle in the plane of sky between the projection of the jet axis and projection of the radial direction of a local fluid element.

The Π_p and χ_p are the local PD and PA, respectively. The Π_p will be expressed as

$$\Pi_p = \frac{\tilde{\alpha}}{(\tilde{\alpha} - 2/3)}, \quad (13)$$

where $\tilde{\alpha}$ is the photon spectral index. $\tilde{\alpha} = \alpha_1$ for $\nu' < \nu'_1$, $\tilde{\alpha} = \alpha_2$ for $\nu'_1 < \nu' < \nu'_2$, and $\tilde{\alpha} = \beta$ for $\nu' > \nu'_2$. Expressions of χ_p can be found in Lan et al. (2016).

The equal arrival time surface (EATS) effect is considered here. The photons, which are emitted from the radius r at the burst-source time t , will arrive the observer at the observer time t_{obs} (Sari 1998; Uhm & Zhang 2016).

$$t_{obs} = \left[t - \frac{r}{c} \cos \theta - t_{on} + \frac{r_{on}}{c} \right] (1+z). \quad (14)$$

For an aligned field in the emission region, PD (Π) and PA (χ) of the jet-shell radiation in GRB prompt phase are

$$\Pi = \frac{\sqrt{Q_\nu^2 + U_\nu^2}}{f_\nu}, \quad (15)$$

and

$$\chi_{pre} = \frac{1}{2} \arctan \left(\frac{U_\nu}{Q_\nu} \right). \quad (16)$$

According to Lan et al. (2018), when $Q_\nu > 0$, the final PA χ equals to χ_{pre} ; when $Q_\nu < 0$, if $U_\nu > 0$ then the PA is $\chi = \chi_{pre} + \pi/2$, if $U_\nu < 0$ then the PA is $\chi = \chi_{pre} - \pi/2$. For a toroidal magnetic field in a roughly constant-velocity shell, U_ν is always 0 because of the axial symmetry and the PD of the jet shell is expressed as

$$\Pi = \frac{Q_\nu}{f_\nu}. \quad (17)$$

If the PD changes its sign, it indicates that the PA is rotated by $\pi/2$.

3. NUMERICAL RESULTS

Time-resolved and time-integrated polarizations in multi-wavelength are studied and the influences of the parameters are also investigated. The orientation of the aligned magnetic field is assumed to be $\delta = \pi/6$ with respect to the projection of the jet axis on the plane of sky. Unless otherwise specified, the values of the following parameters are fixed: $\Gamma_0 = 250$, the jet opening angle $\theta_j = 0.1$ rad, observational angle $\theta_V = \theta_j/2 = 0.05$ rad, $B'_0 = 30$ G, $r_{on} = 10^{14}$ cm, $r_{off} = 3 \times 10^{16}$ cm, $\gamma_{ch}^i = 5 \times 10^4$, $r_0 = 10^{15}$ cm, $\gamma_{ch}^m = 2 \times 10^5$ and $r_m = 2 \times 10^{15}$ cm (Ghirlanda et al. 2018; Lloyd-Ronning et al. 2019; Rouco Escorial et al. 2023; Uhm et al. 2018).

First, we examine the influences of the field decaying index b , mid-energy photon spectral index α_2 , γ_{ch} patterns, and variation of bulk Lorentz factor $\Gamma(r)$ on the multi-band light and polarization curves. The other parameters (except the parameters with fixed values listed above) are listed in Table. 1, and the calculation results are shown in Figure 1.

For all seven models studied in Figure 1, there are two peaks in the light curves of the optical R-band and 5 keV, while there is only one peak at 300 keV and 1 MeV. In the following, we use [1*b*_i] model as an example to study the reasons. Because both the ν_{cool} and ν_{min} will vary with the radius, two critical frequencies at the radius of the maximum local flux on one EATS¹ are shown in Figure 2. We find that the cooling is fast at early stage, and then transit to slow at late times. We define the minimum critical frequency $\nu_1 \equiv \min(\nu_{cool}, \nu_{min})$. The light-curve peaks usually happen when $|\nu - \nu_1|$ reaches its minimum value for a constant maximum flux $F_{\nu, max}$ (Sari et al. 1998). However, the situation becomes complex for a decaying $F_{\nu, max}$. For example,

in the case of 5 keV, $\nu_1 (= \nu_{cool})$ equals to 5 keV at $t_{obs} = 0.74$ s, and the first peak of the 5 keV light curve is just around that time. Similarly, we can see that the second peak occurs near the time when $\nu_1 (= \nu_{min})$ reaches 5 keV. Therefore, for the light curves at 5 keV, the first peak is the fast-cooling peak, and the second is the slow-cooling peak. At optical R-band, the first peak is around the time when $|\nu_1 - \nu|$ reaches its minimum value. Although ν_1 approaches the frequency of the optical R-band at a later time, a decreasing $F_{\nu, max}$ shift the second peak to a relatively earlier time. In the higher energy bands (300 keV and 1 MeV), because of a decaying $F_{\nu, max}$ and the evolution of the ν_1 , there is only one light-curve peak.

It is noted that all calculated PD curves have shallowly rising stages before their steep-decay stages. To interpret this, taken [1*b*_i] model as an example, we plot the PD curves and the evolutions of the corresponding \tilde{f} parameter together as shown in Figure 2. \tilde{f} represents the flux ratio between $\theta\Gamma(r) < 1$ and $\theta\Gamma(r) > 1$ (Lan & Dai 2020).

$$\tilde{f} = \frac{\int_{r_c}^{r_{max}} dF_\nu}{\int_{r_{min}}^{r_c} dF_\nu}, \quad (18)$$

where $r_{min} = \max(r_{on}, r(t_{obs}, \theta = \theta_V + \theta_j))$, $r_{max} = \min(r_{off}, r(t_{obs}, \theta = 0))$ and $\theta\Gamma(r_c) = 1$. It is found that the two quantities are positively correlated except for $\tilde{f} = 0$ or $\tilde{f} = \infty$. With the increase of the \tilde{f} ($\tilde{f} \neq 0$ and $\tilde{f} \neq \infty$), the proportion of the radiation at high latitudes will decrease (i.e., the proportion of the radiation outside the $1/\Gamma$ cone will decrease), then the jet PD will increase and vice versa.

The early high PD phase in the PD curve would be followed by a steep decay phase at late time. Independent of the observational energy band, the beginning time of the late-time steep decay phase of the PD curve is same for the same model. For on-axis observations with $\Gamma_0\theta_j > 1$, PD will decay rapidly when the jet shell expands beyond r_{off} . Therefore, the lasting timescales of the high PD phase is determined by the dynamics of the jet shell. For the same dynamics, i.e., the same bulk-Lorentz-factor variation pattern, the lasting timescales of the high PD phase would be same. The PAs are roughly constants during the main radiation episodes for the four calculated energy band, which is different from a randomly evolving PA in the photosphere model (Parsotan & Lazzati 2022).

The magnetic field strength with a larger b value is larger at small radius and is smaller at large radius. Because the flux density is proportional to $B'^{\frac{2+b}{2}}$ and the emission is roughly uniform in the emitting region at lower energy band (R-band and 5 keV, Granot et al.

¹ Here, the local flux refers to the accumulated flux density at the ring between θ and $\theta + d\theta$.

Table 1. Model Parameters.

Model	b	s (MFC)	γ_{ch} profile	α_2
$1b_i$	1.0	0 (toroidal)	Equation 7	-1.0
$1c_i$	1.25	0 (toroidal)	Equation 7	-1.0
$1d_i$	1.5	0 (toroidal)	Equation 7	-1.0
$1b_i2$	1.0	0 (toroidal)	Equation 7	-3/2
$1b_m$	1.0	0 (toroidal)	Equation 8	-1.0
$2b_i$	1.0	0.35 (aligned)	Equation 7	-1.0
$2b_m$	1.0	0.35 (aligned)	Equation 8	-1.0

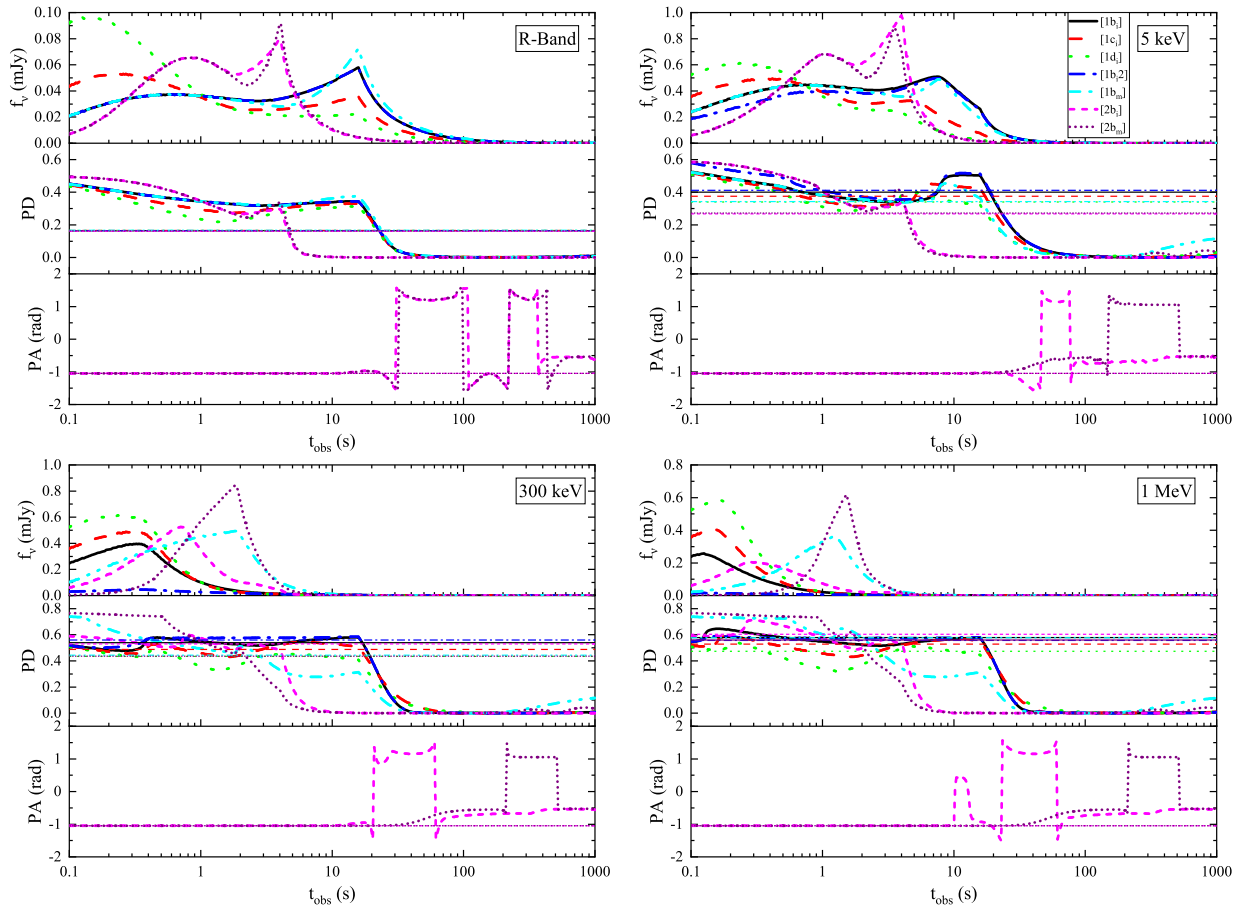


Figure 1. Light curves and polarization evolutions for seven different models. Upper left, upper right, lower left, and lower right panels correspond to the observational energy bands of R-band, 5 keV, 300 keV, and 1 MeV, respectively. In each panel, top, mid and bottom panels show the light, PD and PA curves, respectively. The black solid, red dashed, green dotted, blue dash-dotted, cyan double dot-dashed, magenta short dashed, and purple short dashed lines correspond to the models of $[1b_i]$, $[1c_i]$, $[1d_i]$, $[1b_i2]$, $[1b_m]$, $[2b_i]$, and $[2b_m]$, respectively. The horizontal reference lines show the time-integrated PDs and PAs of the corresponding model.

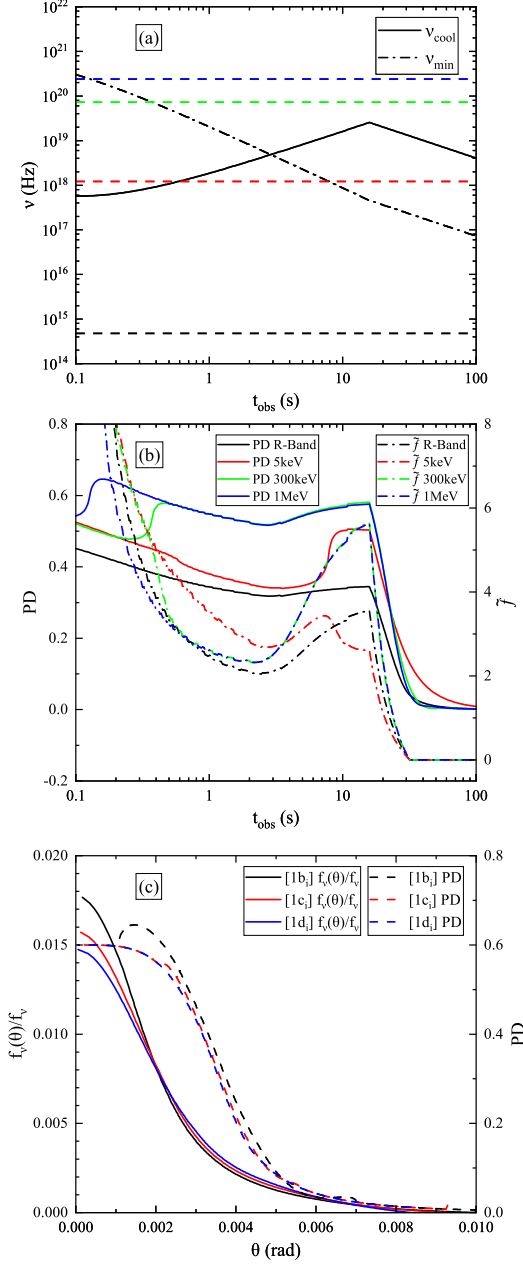


Figure 2. Analysis with the [1b_i] model. (a), evolutions of ν_{cool} and ν_{min} (at the radius of the maximum local flux on one EATS) with the observer time. The black-solid and dash-dot lines correspond to the ν_{cool} and the ν_{min} , respectively. Black, red, green, and blue dashed horizontal reference lines correspond to the observational frequencies of R-band, 5 keV, 300 keV, and 1 MeV, respectively. (b), evolutions of the PD and \tilde{f} parameter with time. The solid and dash-dot lines correspond to the PD and the \tilde{f} curves, respectively. The black, red, green, and blue lines correspond to the observational energy bands of R-band, 5 keV, 300 keV, and 1 MeV, respectively. (c) The distribution of $f_{\nu}(\theta)$ (solid lines) and $PD(\theta)$ (dashed lines) with θ on the EATS of the peak time of the light curve at 300 keV. The black, red, and blue lines correspond to the models of [1b_i], [1c_i], and [1d_i], respectively.

(1999)), the light-curve peak with a larger b value will be higher for early-time emission (see the first light-curve peak in the two low energy band), while it will be lower for late-time emission (see the second light-curve peak).

The profiles of the PD curves are similar and the PD values show slight difference for three b values (corresponding to [1b_i], [1c_i] and [1d_i] models) at each calculated energy-band. The different b value changes the distribution of the local flux density $f_{\nu}(\theta)$ with the radius, resulting in a change in the contribution of the polarized flux at each radius to the total ones. On one EATS, the local PD ($PD(\theta)$, which is the PD of the emission from the ring between θ and $\theta + d\theta$) at smaller θ (i.e., large radius) will approach the maximum local PD Π_p , while $PD(\theta)$ at larger θ (i.e., smaller radius) would be smaller. The larger the index b is, the smaller the $f_{\nu}(\theta)$ at the large radius would be, hence the smaller the contribution of the polarized emission at the large radius to the total one from the whole emitting region. Taking the observational frequency of 300 keV as an example, we plot the distribution of $f_{\nu}(\theta)$ and $PD(\theta)$ with θ at the corresponding peak time of the light curve (see Figure 2). $PD(\theta)$ of small θ is close to the local maximum PD Π_p , while the $f_{\nu}(\theta)$ contribution at small θ of the [1b_i] model is higher than that of the [1c_i] model and the [1d_i] model, so the jet PD of the [1b_i] model is higher. Therefore, the values of time-resolved and time-integrated PD with smaller b will be slightly larger at each calculated energy band.

Because the mid-energy photon spectral index α_2 only affect the local maximum PD Π_p , the Π_p equals to 0.6 for the [1b_i] model and to 0.69 for the [1b_i2] model. The final jet PD would be obtained by the integration on the EATS. So the PD curves of the [1b_i] and the [1b_i2] models are similar in all the calculated energy bands. Therefore, the mid-energy photon spectral index α_2 show slight impacts on the polarizations.

There are five models involving different variation patterns of γ_{ch} in Uhm et al. (2018), as mentioned in Section 2, only i and m models are discussed here. For the i ([1b_i] and [2b_i], with a hard-to-soft E_p evolution mode) and m ([1b_m] and [2b_m], with an intensity-tracking mode) models, the difference of the light curves for the two models becomes obvious in higher energy bands (i.e., 300 keV and 1 MeV). The only difference of the two models is their E_p evolution mode (i.e., the variations of γ_{ch} with the radius). And γ_{ch} is related to the critical frequency ν_{min} , hence the prominent light-curve difference of the two models would be at the energy band above ν_{min} , corresponding to 300 keV and 1 MeV here.

The PD curves and PD spectra of the i and m models had been carefully studied in Lan & Dai (2020). In

their paper, they concluded that PD curves of the two models would in general decay with time and are weakly correlated with the E_p patterns. The conclusions are not changed and it is analysed more meticulously here. At higher energy bands, if $h\nu > E_p$, then the spectral index is β . If $h\nu < E_p$, then the spectral index is α_2 . The local PD Π_p will be larger for a larger spectral index. So for the same observational frequency, the PD of the jet emission with a larger E_p would be smaller in general. Here, the E_p value of the two models at the times of their light-curve peak are both around 300 keV and the E_p value will be larger for the i model before its light-curve peak time, hence compared with the m model, the jet PD will be smaller for i model at early stage.

At early stage (before roughly 0.9 s at which θ equals to 0 at $r = r_0$), compared with the $[1b_i]$ model (a constant-velocity jet), the bulk Lorentz factor of the $[2b_i]$ model (an accelerating jet shell) is smaller (see our setting of the parameters). It will take a longer time for the $[2b_i]$ model to reach the time of the light-curve peak, hence the first light-curve peak at lower energy bands (i.e., R-band and 5 keV here) and the only light-curve peak at higher energy bands (i.e., 300 keV and 1 MeV here) of the $[2b_i]$ model will be later than the corresponding ones for the $[1b_i]$ model. While the second light-curve peak at lower energy bands of the $[2b_i]$ model will be earlier than the corresponding ones for the $[1b_i]$ model. It is because that when $t_{obs} > 0.9$ s the bulk Lorentz factor of the $[2b_i]$ model will be larger than that of the $[1b_i]$ model. The same is for the $[1b_m]$ and $[2b_m]$ models.

We use $[1b_i]$ and $[2b_i]$ models as examples in the following analysis to discuss the effects of the two MFCs. The PD curves of the $[2b_i]$ model (with an aligned field in the emitting region) at lower energy bands (R-band and 5 keV) are similar to that of the $[1b_i]$ model (with a toroidal field in the radiation region). However, its PD evolution trend at higher energy bands (300 keV and 1 MeV) shows obvious differences from that of the $[1b_i]$ model. At early stage, because the jet of the $[1b_i]$ model moves faster than the $[2b_i]$ model, the radiation region for the $[1b_i]$ model will be larger at the same observational time. The field lines becomes less syntropic in the radiation region of the $[1b_i]$ model, while it is always syntropic for an aligned field of the $[2b_i]$ model. Hence, PDs of the $[2b_i]$ model is larger than that of the $[1b_i]$ model.

Because the decay index of the magnetic field, the mid-energy photon spectral index, and the γ_{ch} patten all have slight effect on the jet polarizations, in the following we compare the polarizations of the $[1b_i]$ and $[2b_i]$ models in four energy bands in detail. The variations

of the time-integrated PD with q are shown in Figure 3, and the corresponding light curves and polarization curves are shown in Figures A1 and A2 in the Appendix A. And q is the ratio of θ_V to θ_j . The typical predicted time-integrated PDs will increase with the observational energy band (see Figure 1). It is roughly 17% at optical R-band, roughly 30% at X-rays 5 keV, roughly 50% at 300 keV, and roughly 55% at 1 MeV.

Because an aligned field with a roughly unchanged asymmetry when $q = \theta_V/\theta_j \leq 1$ (on-axis observation) resides in the emission region of the $[2b_i]$ model, its time-integrated PDs when $q \leq 1$ stay as constants. While for the $[1b_i]$ model, with the increase of q When $q \leq 1/(\Gamma_0\theta_j)$, the field in the main radiation region (i.e., within $1/\Gamma_0$) becomes more and more syntropy. And when $1/(\Gamma_0\theta_j) < q < 1 + 1/(\Gamma_0\theta_j)$, the field within $1/\Gamma_0$ keeps roughly syntropy. Hence the time-integrated PD values of $[1b_i]$ model will increase with q when $q \leq 1/(\Gamma_0\theta_j)$ and then be a roughly constant when $1/(\Gamma_0\theta_j) < q < 1 + 1/(\Gamma_0\theta_j)$. The results here are consistent with that in Sui & Lan (2024) and Toma et al. (2009). For off-axis observation ($q = \theta_V/\theta_j > 1$), the variation trends of the time-integrated PD of the two models are different. The time-integrated PD of the $[1b_i]$ model would decrease with q in general in the four energy bands, while after the steep decay phase the time-integrated PD of the $[2b_i]$ model will increase with q .

The variations of the time-integrated PD with both Γ_0 and θ_j are also investigated using $[1b_i]$ and $[2b_i]$ models. The results are shown in Figures 4 and 5, and the corresponding results of the light curves and polarization curves are shown in Figures A3 and A4 in the Appendix A. When Γ_0 increase, the $1/\Gamma$ cone becomes smaller, so the radiation from outside of the $1/\Gamma$ cone will be larger. Therefore, the time-integrated PD would decrease with Γ_0 in general. The time-integrated PD of the $[2b_i]$ model decreases with θ_j in all four energy band, while it will decrease in optical R-band with θ_j and will increase with θ_j in 5 keV, 300 keV and 1 MeV for the $[1b_i]$ model.

4. CONCLUSIONS AND DISCUSSION

In this paper, we use a three-segment power-law spectrum to reconstruct the Stokes parameters of the jet emission in GRB prompt phase. Then the multi-band light curves, polarization curves and the time-integrated polarizations from optical R-band to MeV gamma-rays are studied in detail. The synchrotron emission is assumed here. The MFC in the radiation region is assumed to be large-scale ordered, hence the predicted PD would be the upper limit.

Because of a decaying maximum flux density and the evolution of the minimum critical frequency, the light

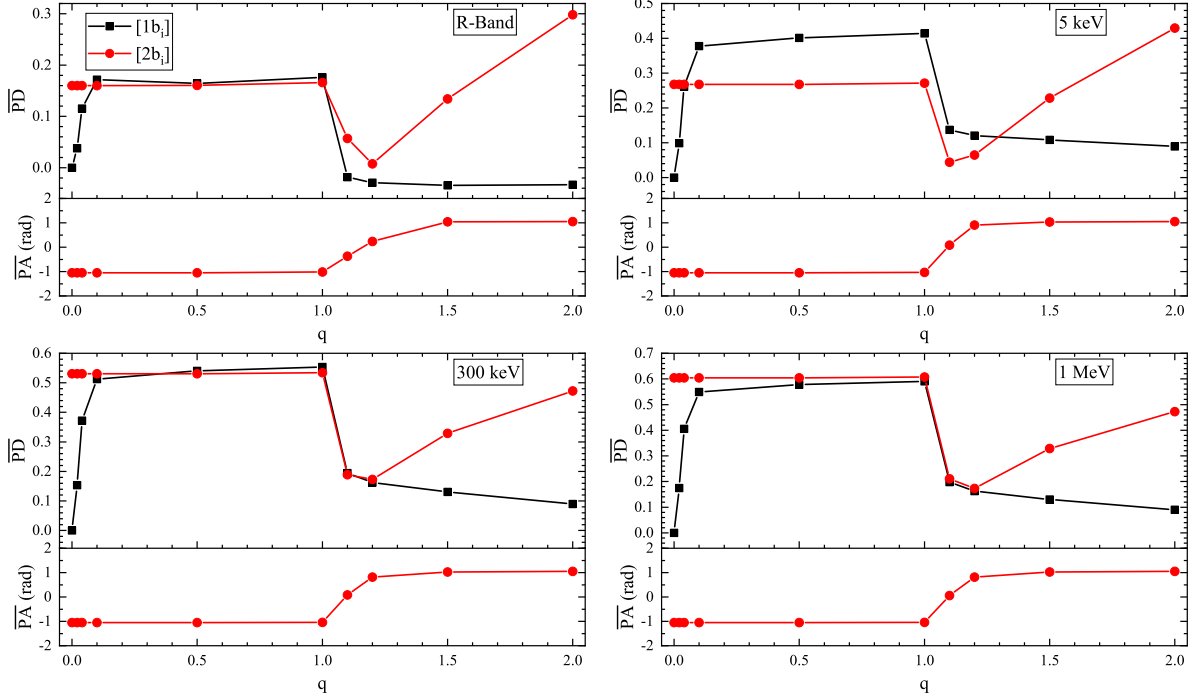


Figure 3. The variations of the time-integrated PD and PA with $q = \theta_V/\theta_j$. Upper-left, upper-right, lower-left, and lower-right panels correspond to the observational energy bands of R-band, 5 keV, 300 keV, and 1 MeV, respectively. The black and red lines correspond to the models of [1*b_i*] and [2*b_i*], respectively.

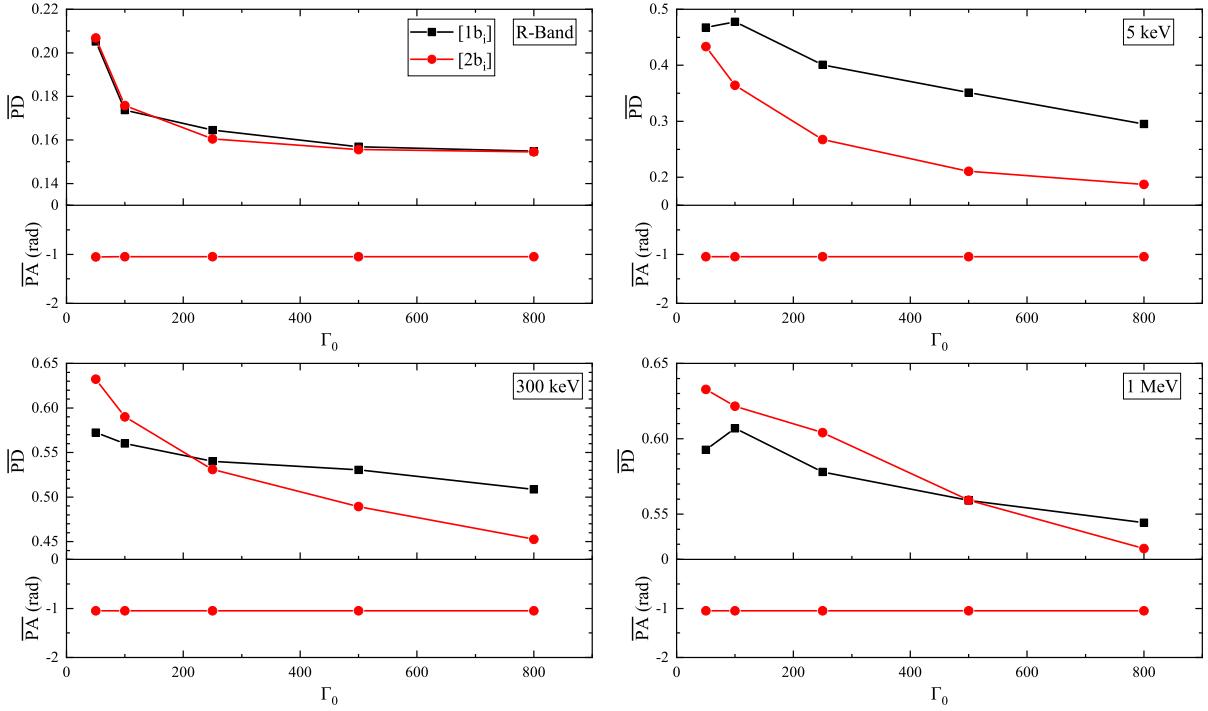


Figure 4. The variations of the time-integrated PD and PA with Γ_0 . Upper-left, upper-right, lower-left, and lower-right panels correspond to the observational energy bands of R-band, 5 keV, 300 keV, and 1 MeV, respectively. The black and red lines correspond to the models of [1*b_i*] and [2*b_i*], respectively.

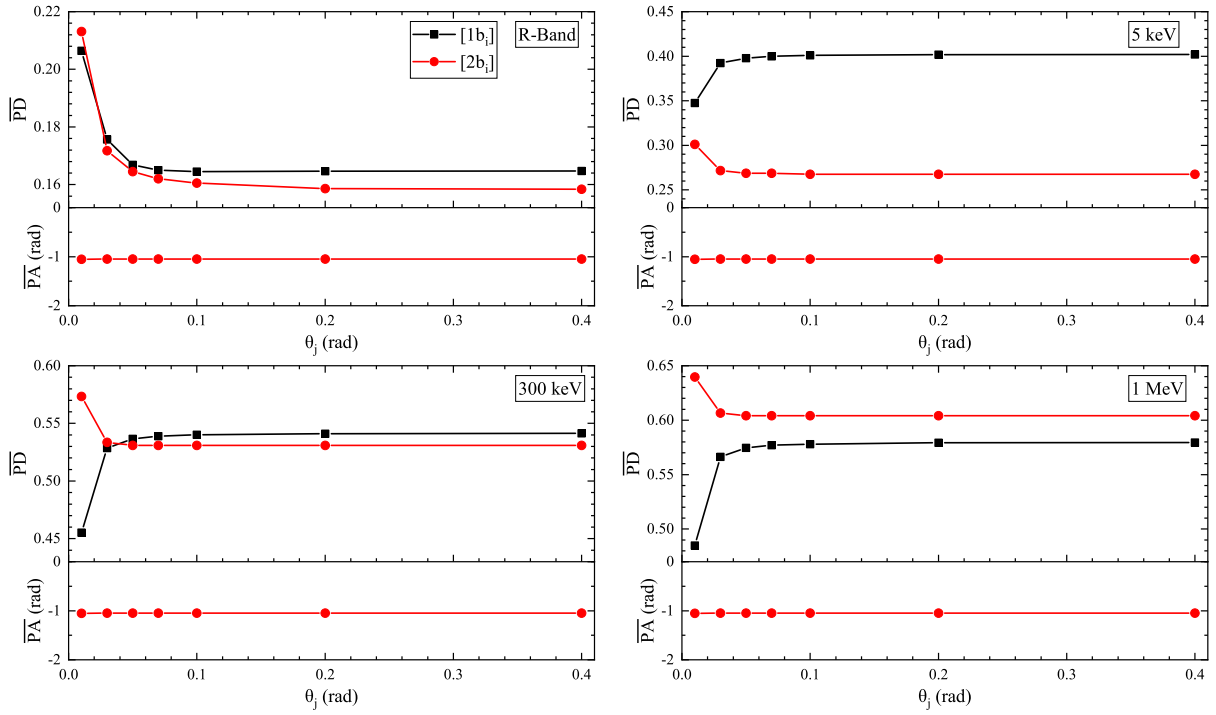


Figure 5. The variations of the time-integrated PD and PA with θ_j . Upper-left, upper-right, lower-left, and lower-right panels correspond to the observational energy bands of R-band, 5 keV, 300 keV, and 1 MeV, respectively. The black and red lines correspond to the models of $[1b_i]$ and $[2b_i]$, respectively.

curves at the lower energy bands (R-band & 5 keV) have two peaks, while there is only one at higher energy bands (300 keV and 1 MeV). A decaying proportion of the emission from the region within $1/\Gamma$ cone will lead to a decrease of the jet PD and vice versa. So the profiles of the PD curves are positively correlated with that of the \tilde{f} parameter (except $\tilde{f} = 0$ and ∞). Due to the evolution of the \tilde{f} parameter, some PD curves decrease at early times, then rises shallowly, and finally continues to decay at late stages. PA is roughly a constant during the main radiation episode at the optical and gamma-ray bands for the synchrotron models here, while it evolves randomly for the photosphere model (Parsotan & Lazzati 2022). Therefore, the synchrotron models and the photosphere model could be distinguished by the time-resolved PA observation.

The product value of Γ_0 and θ_j has a great influence on the polarization. For $\Gamma_0\theta_j > 1$, there will be a long-lasting high PD phase, which would even extend to out of the T_{95} . The reason for this long lasting high PD phase is dynamical. The general profile of the PD curves will not be affected by the concrete peak-energy evolution mode. However, there might be a small PD peak at early stage for the hard-to-soft mode and it is almost unlikely for the intensity-tracking mode (Lan et al. 2021). The time-integrated PD of the synchrotron model would decrease with Γ_0 due to the increase of the radiation outside $1/\Gamma$ cone, while it will increase with the observational energy band. The profile of the $q - \dot{P}D$ curve is similar for the same MFC in the radiation region and is independent of the observational energy band.

At the optical R-band, the time-integrated PD would be roughly 17% in the synchrotron model studied here, while the maximum value of the time-resolved one can reach $\sim 50\%$. The predicted time-integrated PD here is similar to that of the photosphere model (Parsotan & Lazzati 2022). Up till now, there is only one polarization detection in optical band by the MASTER net telescopes during the prompt phase of GRB 160625B (Troja et al. 2017). The detected time-resolved PD at the decay phase of the optical light curve is $\sim 5\%$. Then with the flatten of the optical light curve, it increases to $\sim 8\%$. Theoretically, at the decay phase of the optical light curve, PD also decreases sharply with time down to zero. Both the increase of the observed PD and the flattened light curve in optical band indicate a new radiation component. There are two possible reasons for the detected moderate $\sim 8\%$ PD. One is that the magnetic field in the radiation region is mixed as mentioned in (Troja et al. 2017). The other is because of the mixture of the two offsetting polarized radiation components. In optical band, the Very Large Telescope

(VLT) and Liverpool Telescope (LT) could also do polarization detections. The predicted typical T_{90} of the prompt optical radiation is roughly 100 s and the flux density is around $50 \mu\text{Jy}$, which could be detected by these facilities.

At X-ray band, the only burst with prompt X-ray polarization detection is GRB 221009A and the observed upper limit of the PD ranges from $\sim 55\%$ to $\sim 82\%$ with 99% confidence level by the Imaging X-ray Polarimetry Explorer (IXPE) (Weisskopf et al. 2022; Negro et al. 2023). The predicted time-resolved PD can be as high as 60% and the time-integrated one is roughly around (30–40)% here. Our results here are consistent with the observation. However, because of harsh conditions such observation are quite rare. In the near future, the Low-energy Polarimetry Detector (LPD) on board POLAR-2 (de Angelis & Polar-2 Collaboration 2022) would work. The predicted fluence at X-ray band is about 4×10^{-7} erg cm^{-2} , which might be deficient for polarization analysis. However, for the bright bursts the fluences might reach 4×10^{-5} erg cm^{-2} , which would be sufficient for polarization analysis.

In gamma-ray band, both the time-integrated and time-resolved PD values are predicted to be roughly zero for the photosphere model (Parsotan & Lazzati 2022; Lundman et al. 2018). While the upper limit of the time-integrated one is around 50% for the synchrotron models here. So the models and hence their radiation mechanism can be tested by the PD detection in gamma-ray band. Up till now, we have about 40 bursts with polarization detection in gamma-ray band (Yonetoku et al. 2011, 2012; Zhang et al. 2019; Kole et al. 2020; Chattopadhyay et al. 2022). However, due to the large observational errors the average value of the observed PD can not be determined accurately. The high-energy Polarimetry Detector (HPD) on board POLAR-2 (de Angelis & Polar-2 Collaboration 2022) could distinguish between the 0% polarization and the 10% polarization². Therefore, the detection results of HPD will tell us for most bursts which model will work. The Compton Spectrometer and Imager (COSI), which was planned to launch in 2027, could also detect GRB prompt polarizations (Tomsick et al. 2023). In a two-years mission, it will detect about 40 bursts with polarization observations and the sample would be ampliative. Exciting new phenomena might be found.

² The observed PD values of the bursts by POLAR are concentrated around 10%. However, the 0% polarization can not be ruled out (Zhang et al. 2019; Kole et al. 2020).

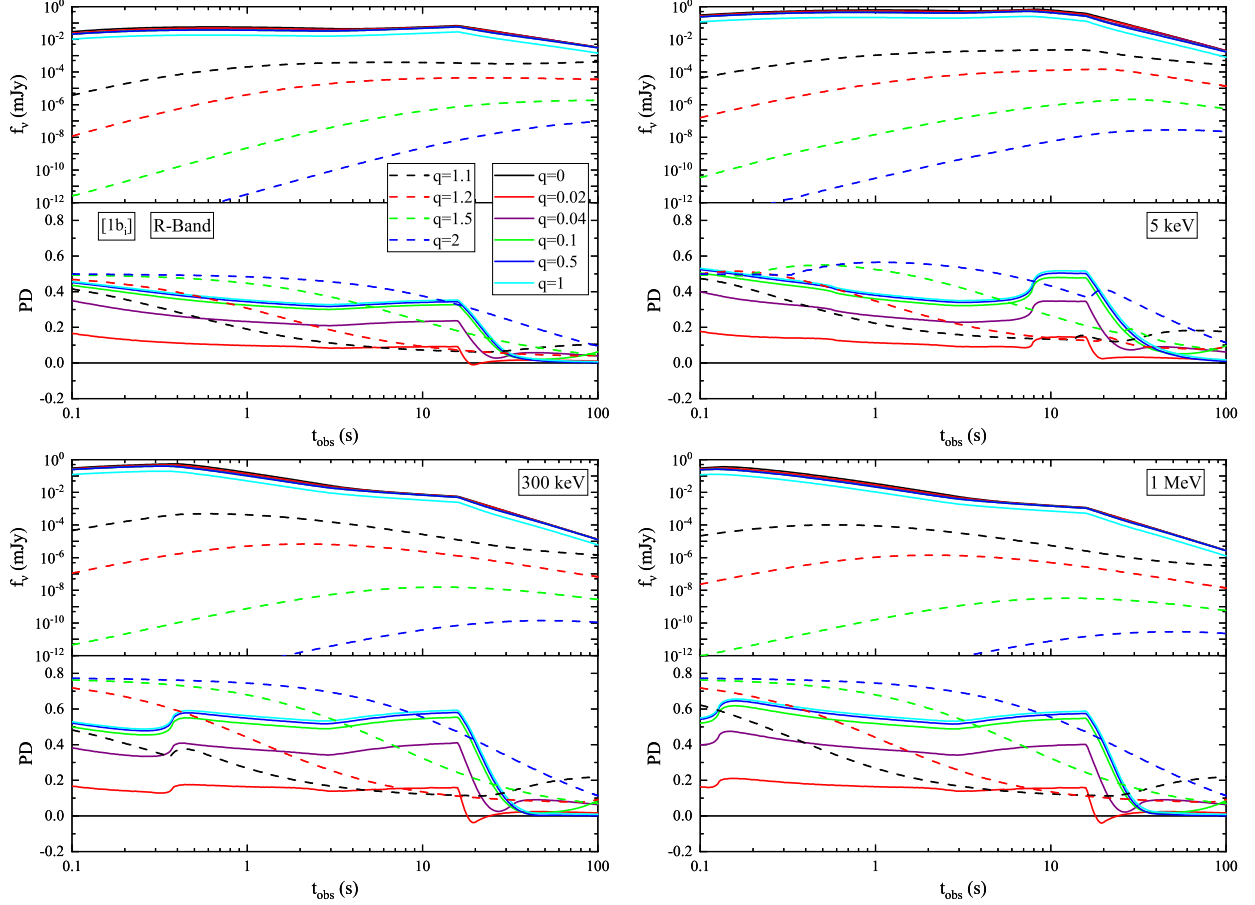


Figure A1. Light curves and polarization evolutions of the $[1b_i]$ model for various $q = \theta_V/\theta_j$ values. Upper-left, upper-right, lower-left, and lower-right panels correspond to the observational energy bands of R-band, 5 keV, 300 keV, and 1 MeV, respectively. In each panel, top and bottom panels show the light and PD curves, respectively. The black, red, purple, green, blue and cyan solid lines correspond to $q = 0, 0.02, 0.04, 0.1, 0.5$ and 1 , respectively. The black, red, green and blue dashed lines correspond to $q = 1.1, 1.2, 1.5$ and 2.0 , respectively.

- 1 We thank the anonymous referee for helpful comments
- 2 that dramatically improved our paper. This work is sup-
- 3 ported by the National Natural Science Foundation of
- 4 China (grant No. 11903014). M.X.L also would like to
- 5 appreciate the financial support from Jilin University.

APPENDIX

A. THE LIGHT CURVES AND POLARIZATION CURVES WITH DIFFERENT PARAMETERS

The impact of the bulk Lorentz factor Γ_0 , jet opening angle θ_j , observational angle θ_V , and MFCs on the light curves and polarizations are investigated. The model parameters follow Table. 1. The orientation of the aligned magnetic field is set to be $\delta = \pi/6$. Other parameters are fixed as follows: $B_0 = 30$ G, $r_{on} = 10^{14}$ cm, $r_{off} = 3 \times 10^{16}$ cm, $\gamma_{ch}^i = 5 \times 10^4$, and $r_0 = 10^{15}$ cm (Uhm et al. 2018).

We fixed $\Gamma_0 = 250$ and $\theta_j = 0.1$ rad, and varied θ_V to calculate the light and polarization curves of the $[1b_i]$ and $[2b_i]$ models. The numerical results are shown in Figures A1 and A2. The PD curves of the $[2b_i]$ model with different q are almost coincide with each other for on-axis observations ($q = \theta_V/\theta_j \leq 1$). While for the $[1b_i]$ model, the PD

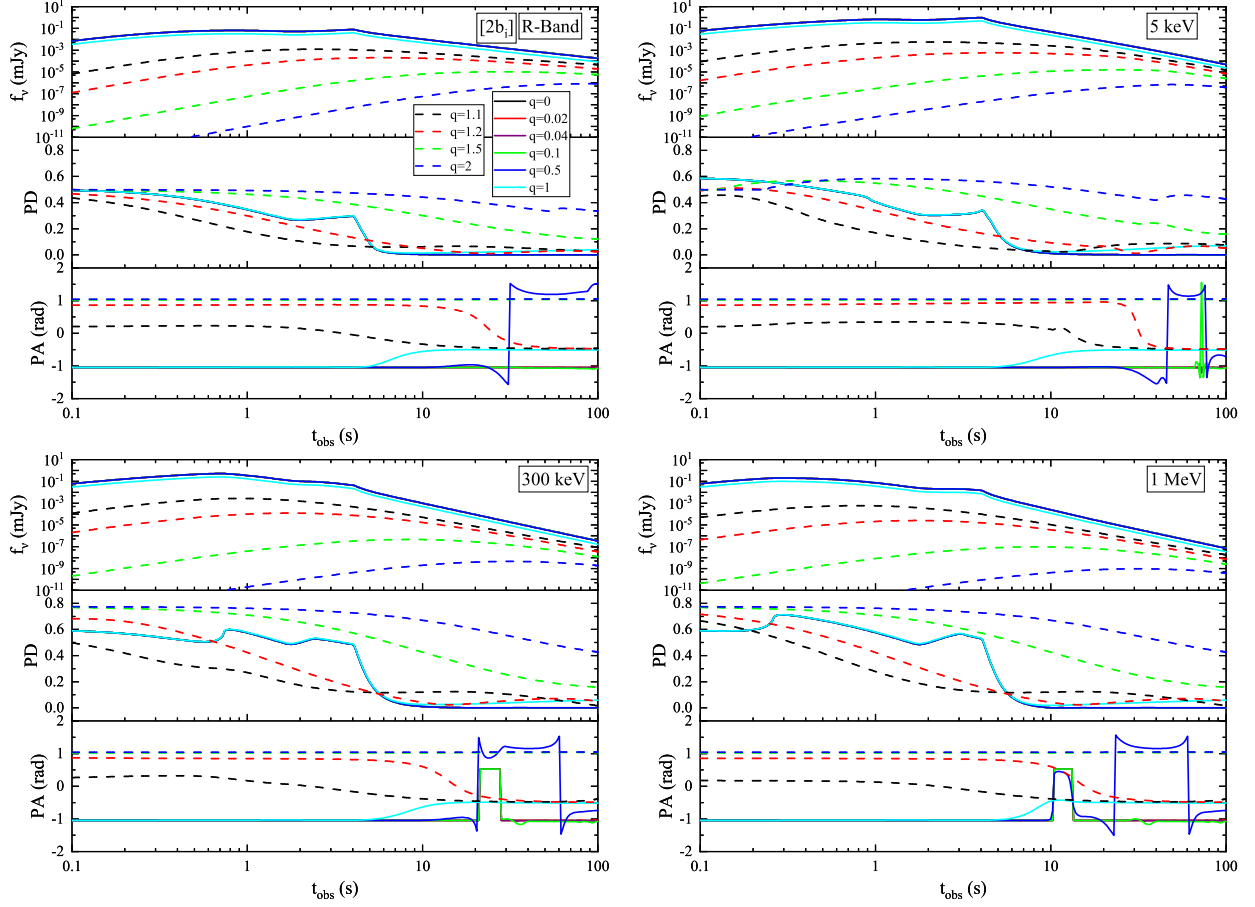


Figure A2. Light curves and polarization evolutions of the $[2b_i]$ model for various $q = \theta_V/\theta_j$ values. Upper-left, upper-right, lower-left, and lower-right panels correspond to the observational energy bands of R-band, 5 keV, 300 keV, and 1 MeV, respectively. In each panel, top, middle, and bottom panels show the light, PD and PA curves, respectively. The black, red, purple, green, blue and cyan solid lines correspond to $q = 0, 0.02, 0.04, 0.1, 0.5$ and 1 , respectively. The black, red, green and blue dashed lines correspond to $q = 1.1, 1.2, 1.5$ and 2.0 , respectively.

values will increase with q when $q \leq 1/(\Gamma_0\theta_j)$ and then be roughly consistent when $1/(\Gamma_0\theta_j) < q < 1 + 1/(\Gamma_0\theta_j)$. There are many abrupt PA rotations or oscillations at late evolution stage. The time and the number of the rotation or the oscillation depend on the computational accuracy when the values of the Stokes parameters becomes small at late stage.

We fixed $\theta_j = 0.1$ rad and $\theta_V = 0.05$ rad, and varied Γ_0 to calculate the light and polarization curves of the $[1b_i]$ and $[2b_i]$ models. The numerical results are shown in Figure A3. The peak of the light curve will move toward large time with a decrease of Γ_0 . And independent of the observational energy band, the lasting timescales of the PD plateau phase will decrease as the Γ_0 increases.

We fixed $\Gamma_0 = 250$ rad and $q = 0.5$, and varied θ_j to study the light and polarization curves of the $[1b_i]$ and $[2b_i]$ models. The numerical results are shown in Figure A4. It is found that the PD curves with $\theta_j = 0.01$ and 0.03 rad will rise at the late stage before the flux density disappears. We then extended the time range to 10000 s, and found the PD curves with other θ_j values have the similar fast rising PD profile at late stage. This is because the field lines in the observed radiation region becomes more syntropic with the shrinking of its area at late stage.

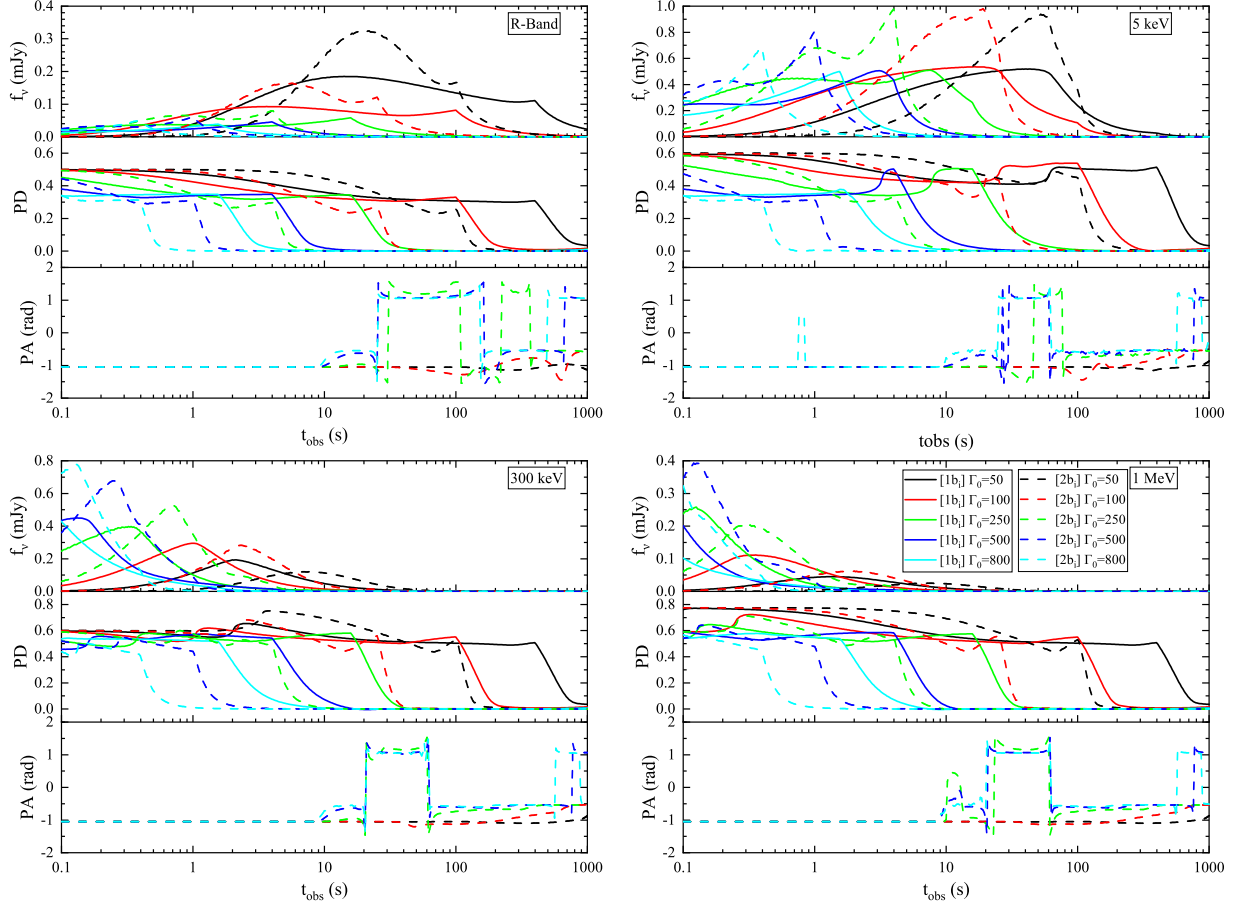


Figure A3. Light curves and polarization evolutions for various bulk Lorentz factor Γ_0 . Upper-left, upper-right, lower-left, and lower-right panels correspond to the observational energy bands of R-band, 5 keV, 300 keV, and 1 MeV, respectively. In each panel, top, middle, and bottom panels show the light, PD and PA curves, respectively. The solid and dashed lines correspond to models of $[1b_i]$ and $[2b_i]$, respectively. The black, red, green, blue, and cyan lines correspond to $\Gamma_0 = 50, 100, 250, 500$ and 800 , respectively.

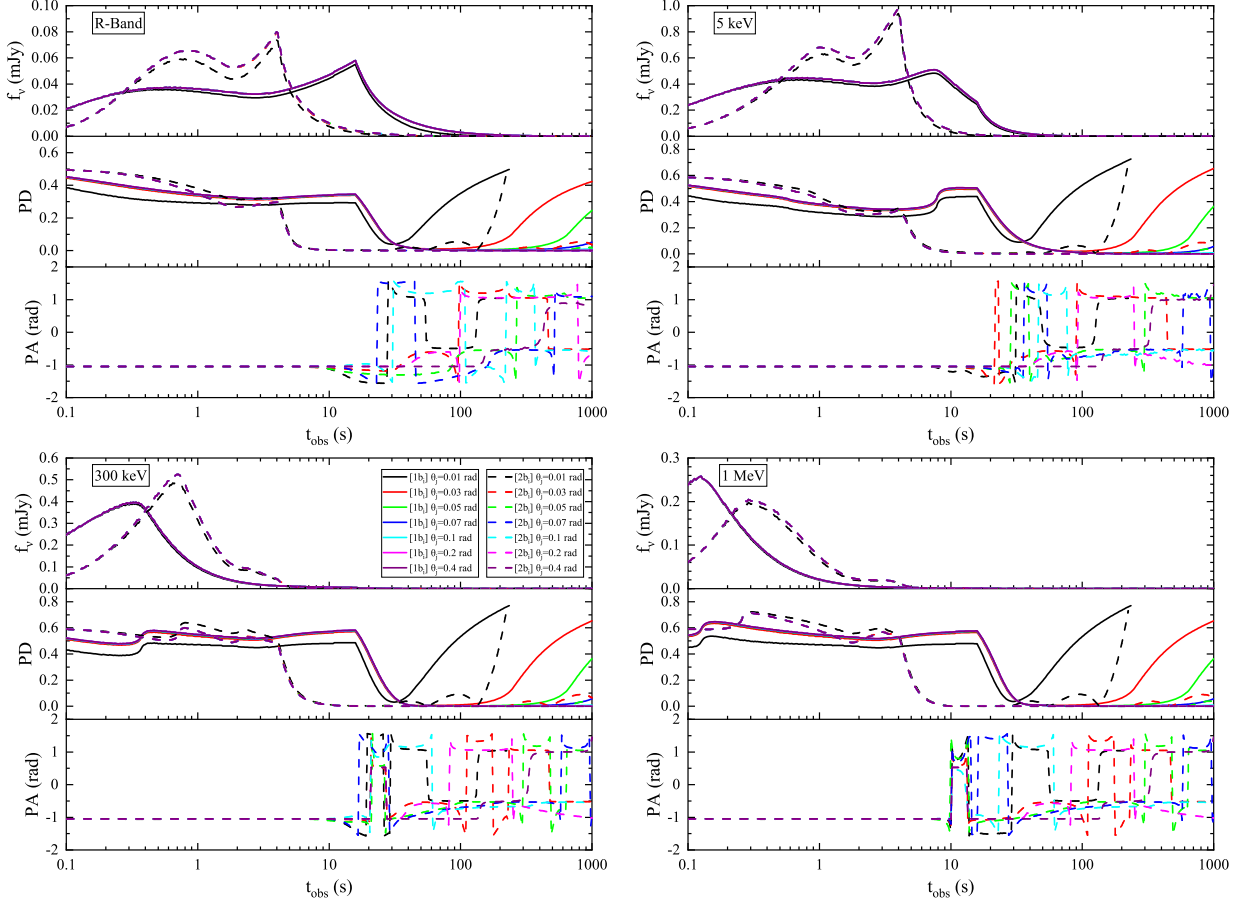


Figure A4. Light curves and polarization evolutions for various jet opening angle θ_j . Upper-left, upper-right, lower-left, and lower-right panels correspond to the observational energy bands of R-band, 5 keV, 300 keV, and 1 MeV, respectively. In each panel, top, middle, and bottom panels show the light, PD and PA curves, respectively. The solid and dashed lines correspond to models of $[1b_i]$ and $[2b_i]$, respectively. The black, red, green, blue, cyan, pink and purple lines correspond to $\theta_j = 0.01, 0.03, 0.05, 0.07, 0.1, 0.2$ and 0.4 rad, respectively.

REFERENCES

- Abbott, B. P., Abbott, R., Abbott, T. D., et al. 2017, *ApJL*, 848, L13
- Band, D., Matteson, J., Ford, L., et al. 1993, *ApJ*, 413, 281
- Bégué, D., Siutsou, I. A., & Vereshchagin, G. V. 2013, *ApJ*, 767, 139
- Beloborodov, A. M. 2011, *ApJ*, 737, 68
- Beniamini, P., & Granot, J. 2016, *MNRAS*, 459, 3635
- Blandford, R. D., & Znajek, R. L. 1977, *MNRAS*, 179, 433
- Bloom, J. S., Kulkarni, S. R., Djorgovski, S. G., et al. 1999, *Nature*, 401, 453
- Chattopadhyay, T., Gupta, S., Iyyani, S., et al. 2022, *ApJ*, 936, 12
- de Angelis, N., & Polar-2 Collaboration. 2022, in 37th International Cosmic Ray Conference. 12-23 July 2021. Berlin, 580
- Drenkhahn, G. 2002, *A&A*, 387, 714
- Eichler, D., & Levinson, A. 2000, *ApJ*, 529, 146
- Ghirlanda, G., Nappo, F., Ghisellini, G., et al. 2018, *A&A*, 609, A112
- Giannios, D. 2008, *A&A*, 480, 305
- Goldstein, A., Veres, P., Burns, E., et al. 2017, *ApJL*, 848, L14
- Granot, J. 2016, *ApJL*, 816, L20
- Granot, J., Piran, T., & Sari, R. 1999, *ApJ*, 513, 679
- Hjorth, J., Sollerman, J., Møller, P., et al. 2003, *Nature*, 423, 847
- Kole, M., De Angelis, N., Berlato, F., et al. 2020, *A&A*, 644, A124
- Lan, M.-X., & Dai, Z.-G. 2020, *ApJ*, 892, 141
- Lan, M.-X., Geng, J.-J., Wu, X.-F., & Dai, Z.-G. 2019, *ApJ*, 870, 96
- Lan, M.-X., Wang, H.-B., Xu, S., Liu, S., & Wu, X.-F. 2021, *ApJ*, 909, 184
- Lan, M.-X., Wu, X.-F., & Dai, Z.-G. 2016, *ApJ*, 816, 73
- . 2018, *ApJ*, 860, 44
- Lazzati, D., Morsony, B. J., & Begelman, M. C. 2009, *ApJL*, 700, L47
- Lazzati, D., Morsony, B. J., Margutti, R., & Begelman, M. C. 2013, *ApJ*, 765, 103
- Lazzati, D., Perna, R., Morsony, B. J., et al. 2018, *PhRvL*, 120, 241103
- Lloyd-Ronning, N. M., Aykutaalp, A., & Johnson, J. L. 2019, *MNRAS*, 488, 5823
- Lundman, C., Pe'er, A., & Ryde, F. 2013, *MNRAS*, 428, 2430
- Lundman, C., Vurm, I., & Beloborodov, A. M. 2018, *ApJ*, 856, 145
- MacFadyen, A. I., Woosley, S. E., & Heger, A. 2001, *ApJ*, 550, 410
- Mazzali, P. A., Deng, J., Tominaga, N., et al. 2003, *ApJL*, 599, L95
- Mészáros, P., & Rees, M. J. 2000, *ApJ*, 530, 292
- Mizuta, A., Nagataki, S., & Aoi, J. 2011, *ApJ*, 732, 26
- Nagakura, H., Ito, H., Kiuchi, K., & Yamada, S. 2011, *ApJ*, 731, 80
- Narayan, R., Paczynski, B., & Piran, T. 1992, *ApJL*, 395, L83
- Negro, M., Di Lalla, N., Omodei, N., et al. 2023, *ApJL*, 946, L21
- Oganesyan, G., Nava, L., Ghirlanda, G., & Celotti, A. 2017, *ApJ*, 846, 137
- . 2018, *A&A*, 616, A138
- Oganesyan, G., Nava, L., Ghirlanda, G., Melandri, A., & Celotti, A. 2019, *A&A*, 628, A59
- Parsotan, T., & Lazzati, D. 2022, *ApJ*, 926, 104
- Pe'er, A., & Ryde, F. 2011, *ApJ*, 732, 49
- Poolakkil, S., Preece, R., Fletcher, C., et al. 2021, *ApJ*, 913, 60
- Ravasio, M. E., Ghirlanda, G., Nava, L., & Ghisellini, G. 2019, *A&A*, 625, A60
- Rees, M. J., & Meszaros, P. 1994, *ApJL*, 430, L93
- Rees, M. J., & Mészáros, P. 2005, *ApJ*, 628, 847
- Rouco Escorial, A., Fong, W., Berger, E., et al. 2023, *ApJ*, 959, 13
- Ruffini, R., Siutsou, I. A., & Vereshchagin, G. V. 2013, *ApJ*, 772, 11
- Rybicki, G. B., & Lightman, A. P. 1979, *Radiative processes in astrophysics*
- Sari, R. 1998, *ApJL*, 494, L49
- Sari, R., Piran, T., & Narayan, R. 1998, *ApJL*, 497, L17
- Spruit, H. C., Daigne, F., & Drenkhahn, G. 2001, *A&A*, 369, 694
- Sui, L.-Q., & Lan, M.-X. 2024, *MNRAS*, arXiv:2403.10718
- Thompson, C. 1994, *MNRAS*, 270, 480
- Toffano, M., Ghirlanda, G., Nava, L., et al. 2021, *A&A*, 652, A123
- Toma, K., Sakamoto, T., Zhang, B., et al. 2009, *ApJ*, 698, 1042
- Tomsick, J. A., Boggs, S. E., Zoglauer, A., et al. 2023, *arXiv e-prints*, arXiv:2308.12362
- Troja, E., Lipunov, V. M., Mundell, C. G., et al. 2017, *Nature*, 547, 425
- Uhm, Z. L., & Zhang, B. 2014, *Nature Physics*, 10, 351
- . 2015, *ApJ*, 808, 33
- . 2016, *ApJ*, 825, 97
- Uhm, Z. L., Zhang, B., & Racusin, J. 2018, *ApJ*, 869, 100

- Weisskopf, M. C., Soffitta, P., Baldini, L., et al. 2022, *Journal of Astronomical Telescopes, Instruments, and Systems*, 8, 026002
- Woosley, S. E. 1993, *ApJ*, 405, 273
- Xu, M., Nagataki, S., Huang, Y. F., & Lee, S. H. 2012, *ApJ*, 746, 49
- Yonetoku, D., Murakami, T., Gunji, S., et al. 2011, *ApJL*, 743, L30
- . 2012, *ApJL*, 758, L1
- Yu, H.-F., Preece, R. D., Greiner, J., et al. 2016, *A&A*, 588, A135
- Zhang, B., & Yan, H. 2011, *ApJ*, 726, 90
- Zhang, S.-N., Kole, M., Bao, T.-W., et al. 2019, *Nature Astronomy*, 3, 258